ACS APPLIED NANO MATERIALS

www.acsanm.org Article

Nonstoichiometric Nanolayered Ni/NiO/Al_2O_3/CrAu Metal–Insulator–Metal Infrared Rectenna

Ayendra Weerakkody, Amina Belkadi, and Garret Moddel*

Cite This: https://dx.doi.org/10.1021/acsanm.0c03012 Read Online

ACCESS | Metrics & More | Article Recommendations | SI Supporting Information

ABSTRACT: Metal–insulator–metal (MIM) diodes with a high cutoff frequency are needed for efficient infrared rectification in optical rectenna systems. Such diodes require low resistance, low capacitance, and high nonlinearity, which are hard to achieve simultaneously. Al_2O_3, with its low dielectric constant of 0.8 at a wavelength of 10.6 μm, offers low capacitance at the price of large diode resistance due to the high barrier it forms with metals. We demonstrate a low-resistance (<2 kΩ) double-insulator Ni/NiO/Al_2O_3/CrAu diode with a small area of 0.025 μm^2. We engineered a subnanometer-thick and nonstoichiometric Al_2O_3, which forms a smaller barrier with the adjacent metal than that for stoichiometric Al_2O_3, resulting in a lower resistance. To verify the expected enhancement in efficiency due to lower resistance and capacitance, we compare the diodes' performance at optical frequencies to what has been published to date. NiO/Al_2O_3 double-insulator–metal–insulator–metal (MI^{2}M) rectennas demonstrate improved total conversion efficiencies and detectivities beyond the best achieved previously for a structure that does not take advantage of resonant tunneling.

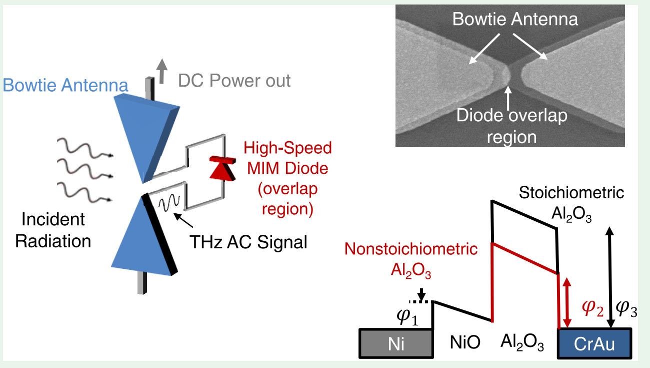

KEYWORDS: *optical rectenna, MIM diodes, 10.6 μm laser, infrared, energy harvesting, thermal rectification*

■ INTRODUCTION AND MOTIVATION

Optical rectenna systems, comprising micron-scale antennas and submicron diodes, require ultrafast diodes with a large cutoff frequency. Metal–insulator–metal (MIM) diodes are good candidates for infrared rectennas since the tunneling time of electrons through thin dielectric films (<5 nm) is on the order of femtoseconds.[2] Such diodes require high nonlinearity at self-biasing voltage, low resistance, and low capacitance. The capacitance is proportional to the dielectric constant, and hence, a particular dielectric of interest for optical rectennas is Al_2O_3. Al_2O_3 offers a small capacitance (C_D) due to its small dielectric constant (ϵ_r) of 0.8 at 28.3 THz.[3] Although Al_2O_3 leads to small diode capacitance, it is important to make sure the diode resistance is small to obtain high cutoff frequencies, $f_c = 1/(2\pi R_D C_D)$. The diode resistance increases roughly exponentially with the insulator thickness and barrier height and has an inverse linear dependence with the device area. The challenge of using Al_2O_3 is the high diode resistance due to a large barrier height at the interface between Al_2O_3 and practical metal contacts. As a consequence, even thin layers of Al_2O_3 in large-area devices still exhibit large resistances (see Table 1). The large resistance values obtained lead to impractically low cutoff frequencies.

Efficient rectification requires nonlinear DC current–voltage $I(V)$ characteristics. Responsivity is an indication of the device nonlinearity and a measure of the DC current generated per watt of incident radiation.[4,5] For our diodes, we are interested in differential resistance ($R_0 = 1/I'$) and responsivity ($\beta_0 = I''/(2I')$)[6] near zero-bias, as the AC voltage applied across the MIM junction (self-biasing voltage) is ≈1 mV. This is because of the poor antenna and coupling efficiencies that reduce the input power delivered to the MIM diode.

In this work, we fabricated the first high-frequency-supporting Al_2O_3-based double-insulator MIM structure (MI^{2}M) exhibiting a relatively low resistance and a moderate zero-bias responsivity while maintaining a small device area (device fabrication process flow is shown in Scheme 1) for low capacitance. We demonstrate the best optical response at 28.3 THz for Al_2O_3-based MIM diodes due to improvements in RC loss and the antenna-diode impedance match. We attained these results by incorporating Al_2O_3 into a Ni/NiO/CrAu MIM structure, as seen in Figure 1. The sub-femtofarad capacitance was achieved by taking advantage of the low dielectric constant of Al_2O_3 at 28.3 THz. To overcome the large barrier created at the interface between Al_2O_3 and most

Received: November 10, 2020
Accepted: February 9, 2021

Table 1. Al_2O_3-Based MIM Diode Literature Survey, Where β_0 Is the Zero-Bias Responsivity and R_0 Is the Zero-Bias Differential Resistance

device(s)	deposition technique	Area (μm^2)	β_0 (A/W)	R_0 (Ω)	normalized R_0[a] (Ω)
$Ti/Al_2O_3/Au$[7]	ALD	0.04	0.44	98 k	156 k
$Al/Al_2O_3/Pt$[8]	plasma oxidation	0.0056	0.40	>22 k	>5 k[b]
$Al/Al_2O_3/ZrCuAlNi$[9]	ALD	800		>1 P	≫1 P
$Al/Al_2O_3/Cr$[10]	ALD	62 500		>1 T	≫1 T
$Cr/Al_2O_3/HfO_2/Cr$[10]	ALD	62 500		>1 T	≫1 T
$Cr/Cr_2O_3/HfO_2/Al_2O_3/Cr$[11]	ALD	62 500		>1 T	≫1 T
$Cr/Cr_2O_3/Al_2O_3/HfO_2/Cr$[11]	ALD	62 500		>1 T	≫1 T
$Al/Al_2O_3/HfO_2/ZrCuAlNi$[9]	ALD	800		>1 P	≫1 P
$Al/HfO_2/Al_2O_3/ZrCuAlNi$[9]	ALD	800		>1 P	≫1 P
$Al/Ta_2O_5/Al_2O_3/ZrCuAlNi$[12]	ALD	800		>1 P	≫1 P
$Al//Al_2O_3/Ta_2O_5/ZrCuAlNi$[12]	ALD	800		>1 P	≫1 P
$Al/Ta_2O_5/Al_2O_3/Al$[13]	ALD	10 000	0.65	2 M	800 G
$Nb/Nb_2O_5/Al_2O_3/Nb$[14]	RF sputtering	10 000	1.40	20 M	8 T
$Nb/Nb_2O_5/Al_2O_3/Ag$[14]	RF sputtering	10 000	2.60	108 M	43 T
$Ni/NiO/Al_2O_3/CrAu$ (this work)	RF Sputtering	0.025	0.31	1.75 k	1.75 k

[a] R_0 normalized to the area of 0.025 μm^2. [b] Current−voltage ($I(V)$) curve not shown in the paper.

Scheme 1. Rectenna Fabrication Process Flow

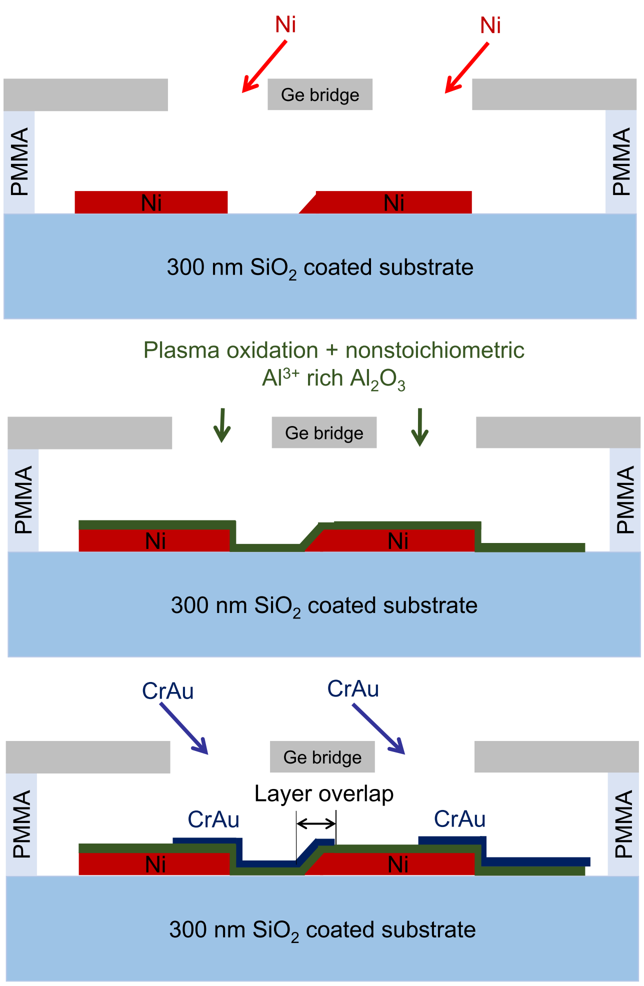

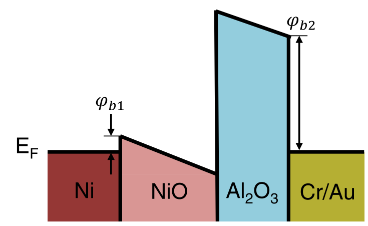

Figure 1. Energy-band profile of double-insulator $Ni/NiO/Al_2O_3/CrAu$ diode with barrier heights ϕ_{b1} = 0.1 eV and ϕ_{b2} = 0.92−1.08 eV. The nominal thicknesses for NiO and Al_2O_3 are 2 and 1.1 nm, respectively.

metals, we modified Al_2O_3 deposition conditions to incorporate more Al^{3+} ions than in the stoichiometric version of it. This was achieved by radio-frequency (RF) sputtering from an Al_2O_3 ceramic target using pure Ar as the carrier gas.[15,16] This results in a higher electron affinity value of 3.26 eV compared to ≈1.4−1.6 eV for thin stoichiometric Al_2O_3[14,17,18] deposited by atomic layer deposition (ALD) and sputtering and hence a lower barrier. A detailed description of the electron affinity determination for Al_2O_3 is presented in the Results and Discussion section. The tunneling probability was enhanced over previous work performed by other groups[7−9,12−14] due to thinner Al_2O_3 (≈1 nm) and smaller barrier heights created with practical metal contacts. A similar concept has been demonstrated by using nonstoichiometric TiO_x in the MIM diode stack, with a junction area of 900 μm^2.[19] This material modification improved current density and device asymmetry compared to a stoichiometric TiO_2-based MIM diode.[19] The electrical characteristics shown for this nonstoichiometric TiO_x-based MIM diode are for low-frequency operation due to RC limitations as it is currently configured.[19] Here, we present the device fabrication process, DC characterization, dominant conduction mechanisms, physical characterization, and finally, optical responses of our MI^2M diode-based rectenna.

■ RESULTS AND DISCUSSION

Fabrication, DC Measurements, and Simulations. A shadow mask process,[1,20] which incorporates a single self-aligned mask layer, was used to fabricate MIM devices with feature sizes on the order of 100 nm (Scheme 1). The patterning process is discussed in detail in Pelz et al.[1] The metals were deposited using thermal evaporation. Metal-1, the first metal in the MIM stack, is a 45 nm thick layer of Ni, and

https://dx.doi.org/10.1021/acsanm.0c03012
ACS Appl. Nano Mater. XXXX, XXX, XXX−XXX

metal-2 is a 3 nm thick layer of Cr followed by 35 nm of Au. For the first oxide, we plasma-oxidized the evaporated Ni surface, estimating a thickness of 2 nm of NiO followed by RF sputter deposition of Al_2O_3 with an estimated thickness of 1.1 nm based on our spectroscopic ellipsometry measurements. Sputtering is known to be less conformal than some other deposition/growth techniques, such as ALD, chemical vapor deposition (CVD), and molecular beam epitaxy (MBE). To confirm our sputter depositions are sufficiently conformal, our group performed cross-sectional high-resolution transmission electron microscopy (TEM) images on MIM rectennas fabricated using the same shadow mask process with plasma-grown NiO and DC reactively sputtered Nb_2O_5.[1] Figure S1 in the Supporting Information shows a scanning electron microscopy (SEM) image of the fabricated rectenna device having a measured diode area of 0.025 μm^2.

Table 1 presents the zero-bias responsivity and zero-bias resistance of the diode. This is the first report of a small resistance (<2 kΩ) Al_2O_3-based MIM diode despite the high Al_2O_3 barrier.[7−14,17]

We used a quantum mechanical diode simulator to simulate the measured $I(V)$ curves of our fabricated diode and extract material parameters such as barrier heights at metal/insulator interfaces, electron effective mass, and thickness. The simulator uses a transfer matrix method to solve a time-independent Schrödinger equation and calculate transmission amplitudes.[21] The simulator provides simulations of single-insulator MIM $I(V)$ curves with high accuracy, but simulating multi-insulator MIM $I(V)$ curves gives ambiguous fitting parameters.[22] This limitation arises for multi-insulator devices due to the unknown voltage division, which in DC is determined by the unknown tunneling resistances of each layer.[22] Hence, only the single-insulator Ni/NiO/CrAu MIM diode fabricated using deposition conditions similar to the structure incorporating Al_2O_3 was simulated to extract the material properties of the Ni/NiO interface. Both measured and simulated $I(V)$ curves for the single-insulator MIM diode are shown in Figure 2.

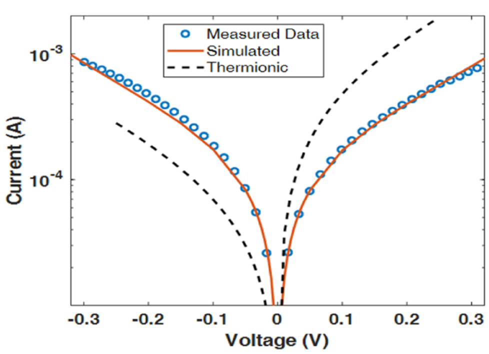

Figure 2. Tunneling and thermionic emission simulations of current−voltage curves used in simulating measured data for a Ni/NiO/CrAu diode.

Based on the simulation, the dominant conduction mechanism for a thin (<2 nm) Ni/NiO/CrAu single-insulator MIM structure is tunneling. In this structure, even though the barrier heights between the metals and insulator are small (<0.1 eV), the oxide is thin enough to be dominated by tunneling electrons over thermionic emission.[23] Table 2 presents the extracted values for work function (Φ), electron affinity (χ), effective electron mass, and effective thicknesses. The non-linear dependence of the transmission probability on barrier shape, in particular, barrier heights and insulator thickness, results in nonlinear diode current−voltage $I(V)$ characteristics.[24,25] Ideally, the bulk material barrier height is $\phi_b = \Phi - \chi$, where Φ is the work function of the metal and χ is the electron affinity of the insulator. The nonstoichiometric and thin nature of these insulators creates different interfacial states between metals and insulators compared to that of bulk interfaces.[26] This results in a change in the effective barrier height from that of the bulk case. Hence, the work function we extracted for CrAu using Ni/NiO/CrAu simulations cannot be used to determine the barrier height at the interface of Al_2O_3/CrAu.[22,27,28] Instead, based on our Fowler−Nordheim calculations,[14,29] we extracted a barrier height of 0.92−1.08 eV between Al_2O_3 and CrAu. In this calculation, we used a thickness of 1.1 nm for Al_2O_3, as measured by variable angle spectroscopic ellipsometry (VASE).

Table 2. Simulation Parameters Extracted for the Measured MIM Diode, Where Φ, χ, t, and m_e Are the Work Function [eV], Electron Affinity [eV], Thickness [nm], and Electron Effective Mass, Respectively

	metals		NiO		
diode	Φ_{Ni}	Φ_{CrAu}	χ	t	m_e
MIM-1	4.9	4.87	4.8	1.5	0.7

The dominant conduction process in the MI^2M structure is tunneling due to the thinness of the insulators (<4 nm).[23] If the carrier transport were limited by a trapping/detrapping process such as the Poole−Frenkel effect, then the transport transit times would be larger than that for tunneling, suppressing high-frequency operation of the rectenna. The results from 28 THz optical measurements that we present later in the paper indicate that such trapping does not appear to be significant in our devices.

Physical Characterization. X-ray photoelectron spectroscopy (XPS) was performed to measure the chemical composition of thin films and extract the valence band offset (VBO) at the oxide interface, and visible/near-IR VASE was performed to extract the thicknesses and band-gap values. These measurements were done to determine the band diagram, which could produce the low resistance from a material perspective. We looked at the NiO/Al_2O_3 interface and material properties of both insulators, with results summarized in Table 3. Using the absorption spectra that we deduced from Tauc plots based on the VASE measurement results, we extracted a smaller band-gap energy of 5.95 eV for Al_2O_3 compared to the bulk value of 6.4−7 eV for thin stoichiometric Al_2O_3.[14,17,30] This is due to the Al^{3+}-rich nonstoichiometric Al_2O_3, as the O/Al atomic ratio was 1.31 compared to the stoichiometric value of 1.5.[31,32] We used Kraut's method[33] to extract the VBO at the interface of NiO/Al2O3 (calculation is shown in the Supporting Information). Then, we combined the VBO with the band-gap values to estimate the conduction band offset (CBO) between NiO and Al_2O_3. The extracted CBO of 1.54 ± 0.3 eV is smaller than the difference between reported χ values (3 eV) for NiO[20] and Al_2O_3.[14,34] An electron affinity value of 3.26 ± 0.3 eV was estimated for nonstoichiometric Al_2O_3, using the electron affinity of NiO and the CBO at the interface of NiO/Al_2O_3 using eq 1

$$\chi_{Al_2O_3} = \chi_{NiO} - \text{CBO} \tag{1}$$

https://dx.doi.org/10.1021/acsanm.0c03012
ACS Appl. Nano Mater. XXXX, XXX, XXX−XXX

Table 3. Summary of Variable Angle Spectroscopic Ellipsometry (VASE) and X-ray Photoelectron Spectroscopy (XPS) Analysis, Where *n* Is the Refractive Index, O/Al Is the Oxygen-to-Aluminum Atomic Ratio, O/Ni Is the Oxygen-to-Nickel Atomic Ratio, VBO Is the Valence Band Offset, and CBO Is the Conduction Band Offset

	VASE (UV−vis−NIR)			XPS			
material/interface	measured thickness (nm)	*n*	band gap (eV)	O/Al	O/Ni	VBO (eV)	CBO (eV)
NiO	1.9	1.98	3.4		0.97		
Al_2O_3	1.1	1.65	5.95	1.31			
Al_2O_3	149.8	1.63	5.98	1.32			
Al_2O_3 (stoichiometric)[30]		1.6	6.4−7	1.5			
NiO/Al_2O_3	1.9/1.1					1.01	1.54

The tunneling probability is enhanced over what it would have been with stoichiometric Al_2O_3 due to the relatively small energy difference between the metal Fermi level and the conduction band edge of Al_2O_3, and the small CBO at the interface of NiO/Al_2O_3.

Given that our Al_2O_3 is nonstoichiometric, we performed mid-IR VASE on 149.8 and 1.1 nm Al_2O_3 to extract the optical properties in the wavelength range from 1.7 to 30 μm, with results shown in Figure 3. The objectives are to see if ϵ_r at 28.3 THz is <1 and to verify that the ϵ_r values of both 1.1 nm Al_2O_3 and 149.8 nm Al_2O_3 are comparable to each other to show that ϵ_r is not thickness-dependent since our diode insulator films are very thin. Initially, we measured the 149.8 nm Al_2O_3 and extracted the thickness and optical properties. Then, the same parameters for Gaussian and Tauc−Lorentzian oscillators used to model the 149.8 nm Al_2O_3 were used to extract the thickness of 1.1 nm Al_2O_3. The thicknesses and ϵ_∞ extracted by mid-IR VASE for both samples are in good agreement (<3% variation) with vis/near-IR VASE measurements. To the best of our knowledge, this is the first measurement of the optical properties of the nonstoichiometric Al_2O_3 performed over a spectral range from 241 nm to 30 μm.

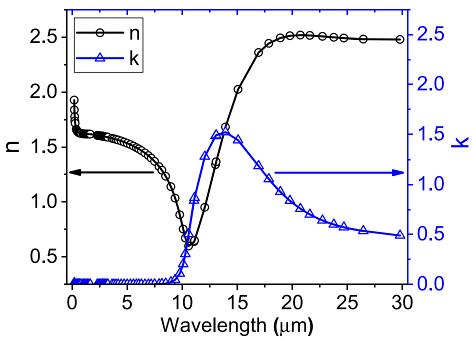

Figure 3. Visible, near-IR, and mid-IR refractive index (*n*), and extinction coefficient (*k*) for 1.1 nm Al_2O_3 and 149.8 nm Al_2O_3 based on mid-IR variable angle spectroscopic ellipsometry measurements.

Optical Results at 28 Thz. To test the operation of MI^2M diode-based rectennas in the infrared, we measured open-circuit voltage (V_{oc}) under illumination from a linearly polarized Access L4SL infrared CO_2 laser at 10.6 μm, with results shown in Figure 4. Assuming that the effective area of the antenna is the area of the circle that encloses it, the input power (P_{in}) to the diode was 0.72 μW since the beam intensity was 3×10^4 W m^{-2} over an area of 24 μm^2. For a response due to rectified current from the antenna, we would expect a larger V_{oc} when the polarization angle of the beam is parallel to the antenna axis (see the inset of Figure 4) than when the polarization angle is 90° or perpendicular to the antenna axis. The measured polarization-dependent V_{oc} yielded a cosine-squared relationship, as expected. We also confirmed that our diode oxides were not damaged, as a polarization-dependent V_{oc} is expected due to the Seebeck effect if the insulators were damaged.[35−37] The DC $I(V)$ measurements were performed both before and after the optical measurement to confirm the insulators were undamaged. To the best of our knowledge, these are the best optical measurements in terms of the magnitude and peak-to-valley ratio reported due to rectification as opposed to thermal effects.[7,8,35,37]

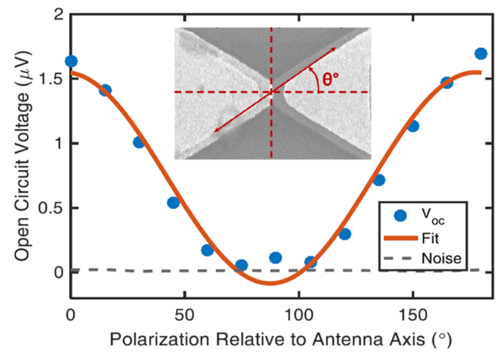

Figure 4. Optical measurements at 10.6 μm of V_{oc} as a function of the polarization angle for the Ni/NiO/Al_2O_3/CrAu rectenna.

In multi-insulator diodes, high-frequency $I(V)$ characteristics differ from those at DC due to the difference in voltage division across the insulators.[22] Hence, it is necessary to measure both V_{oc} and I_{sc} under illumination to evaluate the rectenna's high-frequency performance. We measured V_{oc} and I_{sc} for both MIM and MI^2M rectenna structures and performed analysis to eliminate parasitic series resistances, as explained in detail in the Supplementary Information (Section 7) of Belkadi et al.[22] The measured I_{sc} values for the MIM and MI^2M were 0.81 and 0.39 nA, respectively. The high-frequency resistance of the MI^2M structure increased by 61.5%, while the change in the MIM structure was only 11%. In the MI^2M structure, the larger resistance can be explained as resulting from a reduced potential drop across the NiO at 28.3 THz as compared to that at DC. This explanation is consistent with our simulations.[22] Using these measured parameter resistance values, we calculated the coupling efficiency (η_c), the overall conversion efficiency (η), and detectivity (D^*) for both MIM- and MI^2M-based rectennas.[22] The results from the high-frequency analysis for both structures are summarized in Table 4. We observed an enhancement in η_c, η, and D^* by factors of 2.4, 7, and 15.5, respectively, compared to our lower resistance (702 Ω) Ni/NiO/CrAu MIM diode. Usually, these parameters decrease

https://dx.doi.org/10.1021/acsanm.0c03012
ACS Appl. Nano Mater. XXXX, XXX, XXX−XXX

Table 4. Summary of Analysis of Optical Measurements for the Ni/NiO/Al_2O_3/CrAu Rectenna at 10.6 μm (R_0 Is the Zero-Bias Differential Resistance, η_c Is the Coupling Efficiency, η Is the Overall Conversion Efficiency, and D^* Is Detectivity)

diode	R_0 (high frequency) (Ω)	η_c (%)	η (%)	D^* (cm $Hz^{1/2}$ W^{-1})
Ni/NiO/CrAu	702	2.9×10^{-1}	5.4×10^{-9}	1.1×10^{4}
Ni/NiO/Al_2O_3/CrAu	2826	7×10^{-1}	3.7×10^{-8}	1.7×10^{5}

with increasing resistance. In this case, we ascribe this improvement in the MI^2M structure to the reduction in the capacitance by including the low-dielectric-constant Al_2O_3 layer.

CONCLUSIONS

We fabricated and characterized a low-resistance Al_2O_3-based MI^2M diode with a zero-bias responsivity of approximately 0.5 A/W and a zero-bias resistance of 1.75 kΩ in DC, with the proven high-frequency operation. We achieved this by modifying the chemical composition of Al_2O_3 without causing detrimental effects to the conduction tunneling process or to the optical properties. These changes were verified experimentally by XPS and UV−vis−near-IR/mid-IR VASE measurements. Because of the reduced resistance and the low capacitance resulting from a low dielectric constant of Al_2O_3 at 28.3 THz, the rectenna exhibited an improvement in the overall conversion efficiency by 3 orders of magnitude beyond the state-of-the-art for a lumped element rectenna configuration,[1,7] with a coupling efficiency of 0.7% and a detectivity of 1.7×10^5 cm $Hz^{1/2}$ W^{-1} at 28.3 THz.

METHODS

Fabrication. A modified germanium shadow mask process was used to fabricate MIM diode structures with 100 nm feature sizes.[1] The first step of the process was to spin-coat ∼260 nm poly(methylmethacrylate) (PMMA) on a highly resistive p-type Si substrate coated with the thermally grown 300 nm SiO_2. Next, 60 nm of germanium was evaporated on PMMA. The pattern was printed on the surface of the wafer by an ASML 5500 248 nm DUV stepper. Afterward, the pattern was transferred into the germanium layer with a CF_4 inductively coupled-reactive ion etch followed by an O_2 plasma etch to remove the underlayer of PMMA. The O_2 plasma was run at a relatively high pressure of 350−400 mTorr to achieve an undercut of at least 250 nm under the germanium bridge, resulting in widths varying from 235 to 260 nm.

Experimental Setup. The rectenna was illuminated with a 10.6 μm linearly polarized radiation from pulsed Synrad 48-1SWJ or continuous wave Access L4SL CO_2 lasers. The Synrad 48-1SWJ laser was pulse-width-modulated by an Agilent 33220A function generator at 20 kHz. To monitor the noise level under dark conditions, the laser beam passed through a ThorLabs SH05 shutter. A half-wave plate (ThorLabs PRM1Z8) was used in the optical path to rotate the laser polarization with respect to the antenna axis. The reference signal to the lock-in amplifier (SR830) was generated by a mechanical chopper at 1.7 kHz.

ASSOCIATED CONTENT

Supporting Information

The Supporting Information is available free of charge at https://pubs.acs.org/doi/10.1021/acsanm.0c03012.

Additional information on characterization of the single-insulator and double-insulator diodes, including diode areas from SEM images; exponential fitting parameters; band diagram study; and efficiency and detectivity calculation (PDF)

AUTHOR INFORMATION

Corresponding Author

Garret Moddel − *Department of Electrical, Computer and Energy Engineering, University of Colorado, Boulder, Colorado 80309, United States;* orcid.org/0000-0002-1397-0319; Email: moddel@colorado.edu

Authors

Ayendra Weerakkody − *Department of Electrical, Computer and Energy Engineering, University of Colorado, Boulder, Colorado 80309, United States;* orcid.org/0000-0003-2370-5698

Amina Belkadi − *Department of Electrical, Computer and Energy Engineering, University of Colorado, Boulder, Colorado 80309, United States;* orcid.org/0000-0001-6575-5197

Complete contact information is available at: https://pubs.acs.org/10.1021/acsanm.0c03012

Notes

The authors declare no competing financial interest.

ACKNOWLEDGMENTS

The authors would like to thank David Doroski for assistance with fabrication of the structures and John Stearns and Brad Pelz for valuable discussions and helpful comments. This work was carried out in part under contract from RedWave Energy Inc. and funded in part by the Advanced Research Projects Agency-Energy (ARPA-E), U.S. Department of Energy, under Award Number DE-AR0000676. A portion of the fabrication was carried out at the UCSB Nanofabrication Facility. G.M. holds stock in RedWave Energy, Inc.

REFERENCES

(1) Pelz, B.; Moddel, G. Demonstration of distributed Capacitance Compensation in a Metal-Insulator-Metal Infrared Rectenna incorporating a Traveling-Wave Diode at 10.6 μm. *J. Appl. Phys.* **2019**, *125*, No. 234502.

(2) Nguyen, H.; Cutler, P.; Feuchtwang, T.; Huang, Z.-H.; Kuk, Y.; Silverman, P.; Lucas, A.; Sullivan, T. Mechanisms of Current Rectification in an STM Tunnel Junction and the Measurement of an Operational Tunneling Time. *IEEE Trans. Electron Devices* **1989**, *36*, 2671−2678.

(3) Kischkat, J.; Peters, S.; Gruska, B.; Semtsiv, M.; Chashnikova, M.; Klinkmüller, M.; Fedosenko, O.; Machulik, S.; Aleksandrova, A.; Monastyrskyi, G.; Flores, Y.; Masselink, W.T. Mid-infrared optical properties of thin films of aluminum oxide, titanium dioxide, silicon dioxide, aluminum nitride, and silicon nitride. *Appl. Opt.* **2012**, *51*, 6789−6798.

(4) Sanchez, A.; Davis, C. F.; Liu, K. C.; Javan, A. The MOM tunneling diode: Theoretical estimate of its performance at microwave and infrared frequencies. *J. Appl. Phys.* **1978**, *49*, 5270−5277.

(5) Tucker, J. R.; Millea, M. F. Photon detection in nonlinear tunneling devices. *Appl. Phys. Lett.* **1978**, *33*, 611−613.

(6) Cowley, A. M.; Sorensen, H. O. Quantitative Comparison of Solid-State Microwave Detectors. *IEEE Trans. Microwave Theory Tech.* **1966**, *14*, 588−602.

(7) Jayaswal, G.; Belkadi, A.; Meredov, A.; Pelz, B.; Moddel, G.; Shamim, A. Optical rectification through an Al 2 O 3 based MIM passive rectenna at 28.3 THz. *Mater. Today Energy* **2018**, *7*, 1−9.

(8) Bean, J. A.; Weeks, A.; Boreman, G. D. Performance Optimization of Antenna-Coupled Al AlO Pt Tunnel Diode Infrared Detectors. *IEEE J. Quantum Electron.* **2011**, *47*, 126−135.

(9) Alimardani, N.; Conley, J. F., Jr. Step tunneling enhanced asymmetry in asymmetric electrode metal-insulator-insulator-metal tunnel diodes. *Appl. Phys. Lett.* **2013**, *102*, No. 143501.

(10) Maraghechi, P.; Foroughi-Abari, A.; Cadien, K.; Elezzabi, A. Y. Enhanced rectifying response from metal-insulator-insulator-metal junctions. *Appl. Phys. Lett.* **2011**, *99*, No. 253503.

(11) Maraghechi, P.; Foroughi-Abari, A.; Cadien, K.; Elezzabi, A. Y. Observation of resonant tunneling phenomenon in metal-insulator-insulator-insulator-metal electron tunnel devices. *Appl. Phys. Lett.* **2012**, *100*, No. 113503.

(12) Alimardani, N.; Conley, J. F., Jr. Enhancing metal-insulator-insulator-metal tunnel diodes via defect enhanced direct tunneling. *Appl. Phys. Lett.* **2014**, *105*, No. 082902.

(13) Weerakkody, A.; Sedghi, N.; Mitrovic, I.; van Zalinge, H.; Noureddine, I. N.; Hall, S.; Wrench, J.; Chalker, P.; Phillips, L.; Treharne, R.; Durose, K. Enhanced low voltage nonlinearity in resonant tunneling metal-insulator-insulator-metal nanostructures. *Microelectron. Eng.* **2015**, *147*, 298−301.

(14) Mitrovic, I.; Weerakkody, A.; Sedghi, N.; Ralph, J.; Hall, S.; Dhanak, V.; Luo, Z.; Beeby, S. Controlled modification of resonant tunneling in metal-insulator-insulator-metal structures. *Appl. Phys. Lett.* **2018**, *112*, No. 012902.

(15) Voigt, M.; Sokolowski, M. Electrical properties of thin rf sputtered aluminum oxide films. *Mater. Sci. Eng. B* **2004**, *109*, 99−103.

(16) Taylor, T. R.; Hansen, P. J.; Pervez, N.; Acikel, B.; York, R. A.; Speck, J. S. Influence of stoichiometry on the dielectric properties of sputtered strontium titanate thin films. *J. Appl. Phys.* **2003**, *94*, 3390−3396.

(17) Alimardani, N.; King, S. W.; French, B. L.; Tan, C.; Lampert, B. P.; Conley, J. oF., Jr. Investigation of the impact of insulator material on the performance of dissimilar electrode metal-insulator-metal diodes. *J. Appl. Phys.* **2014**, *116*, No. 024508.

(18) Chathuranga, D. A. D. Engineered High-k Oxides. Ph.D. thesis, University of Liverpool, 2016.

(19) Matsuura, D.; Shimizu, M.; Yugami, H. High-current density and high-asymmetry MIIM diode based on oxygen-non-stoichiometry controlled homointerface structure for optical rectenna. *Sci. Rep.* **2019**, *9*, No. 19639.

(20) Hobbs, P. C.; Laibowitz, R. B.; Libsch, F. R.; LaBianca, N. C.; Chiniwalla, P. P. Efficient waveguide-integrated tunnel junction detectors at 1.6 μm. *Opt. Express* **2007**, *15*, 16376−16389.

(21) Grover, S.; Moddel, G. Engineering the current-voltage characteristics of metal-insulator-metal diodes using double-insulator tunnel barriers. *Solid-State Electron.* **2012**, *67*, 94−99.

(22) Belkadi, A.; Weerakkody, A.; Moddel, G. Large Errors from Assuming Equivalent DC and High-Frequency Electrical Characteristics in Metal-Multiple-Insulator-Metal Diodes. *ACS Photonics* **2018**, *5*, 4776−4780.

(23) Simmons, J. G. Potential barriers and emission-limited current flow between closely spaced parallel metal electrodes. *J. Appl. Phys.* **1964**, *35*, 2472−2481.

(24) Stratton, R. Volt-current characteristics for tunneling through insulating films. *J. Phys. Chem. Solids* **1962**, *23*, 1177−1190.

(25) Simmons, J. G. Generalized Formula for the Electric Tunnel Effect between Similar Electrodes Separated by a Thin Insulating Film. *J. Appl. Phys.* **1963**, *34*, 1793−1803.

(26) Jenkins, M. A.; Klarr, T.; Austin, D. Z.; Li, W.; Nguyen, N. V.; Conley, J. F., Jr. Assessment of Energy Barriers Between ZrCuAlNi Amorphous Metal and Atomic Layer Deposition Insulators Using Internal Photoemission Spectroscopy. *Phys. Status Solidi RRL* **2018**, *12*, No. e1700437.

(27) Herner, S.; Weerakkody, A.; Belkadi, A.; Moddel, G. High performance MIIM diode based on cobalt oxide/titanium oxide. *Appl. Phys. Lett.* **2017**, *110*, No. 223901.

(28) Herner, S. B.; Belkadi, A.; Weerakkody, A.; Pelz, B.; Moddel, G. Responsivity-resistance relationship in MIIM diodes. *IEEE J. Photovoltaics* **2017**, 499−504.

(29) Fowler, R. H.; Nordheim, L. Electron emission in intense electric fields. *Proc. R. Soc. London, Ser. A* **1928**, *119*, 173−181.

(30) Filatova, E. O.; Konashuk, A. S. Interpretation of the Changing the Band Gap of Al2O3 Depending on Its Crystalline Form: Connection with Different Local Symmetries. *J. Phys. Chem. C* **2015**, *119*, 20755−20761.

(31) Tan, E.; Mather, P. G.; Perrella, A. C.; Read, J. C.; Buhrman, R. A. Oxygen stoichiometry and instability in aluminum oxide tunnel barrier layers. *Phys. Rev. B* **2005**, *71*, No. 161401.

(32) Haeberle, J.; Henkel, K.; Gargouri, H.; Naumann, F.; Gruska, B.; Arens, M.; Tallarida, M.; Schmeier, D. Ellipsometry and XPS comparative studies of thermal and plasma enhanced atomic layer deposited Al2O3-films. *Beilstein J. Nanotechnol.* **2013**, *4*, 732−742.

(33) Kraut, E. A.; Grant, R. W.; Waldrop, J. R.; Kowalczyk, S. P. Semiconductor core-level to valence-band maximum binding-energy differences: Precise determination by x-ray photoelectron spectroscopy. *Phys. Rev. B* **1983**, *28*, 1965−1977.

(34) Yeo, Y.-C.; King, T.-J.; Hu, C. Metal-dielectric band alignment and its implications for metal gate complementary metal-oxide-semiconductor technology. *J. Appl. Phys.* **2002**, *92*, 7266−7271.

(35) Bean, J. A.; Tiwari, B.; Bernstein, G. H.; Fay, P.; Porod, W. Thermal infrared detection using dipole antenna-coupled metal-oxide-metal diodes. *J. Vac. Sci. Technol., B: Microelectron. Nanometer Struct.–Process., Meas., Phenom.* **2009**, *27*, 11−14.

(36) Tiwari, B.; Bean, J. A.; Szakmány, G.; Bernstein, G. H.; Fay, P.; Porod, W. Controlled etching and regrowth of tunnel oxide for antenna-coupled metal-oxide-metal diodes. *J. Vac. Sci. Technol., B: Microelectron. Nanometer Struct.–Process., Meas., Phenom.* **2009**, *27*, 2153−2160.

(37) Bareiß, M.; Krenz, P. M.; Szakmany, G. P.; Tiwari, B. N.; Kalblein, D.; Orlov, A. O.; Bernstein, G. H.; Scarpa, G.; Fabel, B.; Zschieschang, U.; Klauk, H.; Porod, W.; Lugli, P. Rectennas revisited. *IEEE Trans. Nanotechnol.* **2013**, *12*, 1144−1150.

https://dx.doi.org/10.1021/acsanm.0c03012
ACS Appl. Nano Mater. XXXX, XXX, XXX−XXX